White Rose Research Online

eprints@whiterose.ac.uk
https://eprints.whiterose.ac.uk
Universities of Leeds, Sheffield and York

Deposited via The University of Sheffield.

White Rose Research Online URL for this paper:
https://eprints.whiterose.ac.uk/id/eprint/169421/

Version: Accepted Version

Article:
Xia, D., Xu, Y., Mannering, J. et al. (2021) Tuning the electrical and solar thermal heating efficiencies of nanocarbon aerogels. Chemistry of Materials, 33 (1). pp. 392-402. ISSN: 0897-4756

https://doi.org/10.1021/acs.chemmater.0c04166

This document is the Accepted Manuscript version of a Published Work that appeared in final form in Chemistry of Materials, copyright © American Chemical Society after peer review and technical editing by the publisher. To access the final edited and published work see https://doi.org/10.1021/acs.chemmater.0c04166

Reuse
Items deposited in White Rose Research Online are protected by copyright, with all rights reserved unless indicated otherwise. They may be downloaded and/or printed for private study, or other acts as permitted by national copyright laws. The publisher or other rights holders may allow further reproduction and re-use of the full text version. This is indicated by the licence information on the White Rose Research Online record for the item.

Takedown
If you consider content in White Rose Research Online to be in breach of UK law, please notify us by emailing eprints@whiterose.ac.uk including the URL of the record and the reason for the withdrawal request.

UNIVERSITY OF LEEDS
University of Sheffield
UNIVERSITY of York

Tuning the Electrical and Solar-Thermal Heating Efficiencies of Nanocarbon Aerogels

Dong Xia, Yifei Xu, Jamie Mannering, Xiaolong Ma, Mohammed Ismail, Duncan Borman, Daniel Baker, Mohammed Pourkashanian and Robert Menzel*

D. Xia, Dr. Y. Xu, J. Mannering, Dr. R. Menzel
School of Chemistry, University of Leeds, Leeds, UK.
E-mail: cmdx@leeds.ac.uk

X. Ma
School of Chemical and Process Engineering, University of Leeds, Leeds, UK.

Dr. M. Ismail, M. Pourkashanian
Department of Mechanical Engineering, The University of Sheffield, Sheffield, UK.

Dr. D. Borman
School of Civil Engineering, University of Leeds, Leeds, UK.

Dr. D. Baker
School of Physics and Astronomy, University of Leeds, LS2 9JT, Leeds, UK

Keywords: nanocarbon aerogels, tunable microstructures, thermal properties, Joule-heating, solar steam generation

Abstract

Two different types of carbon nanotube (CNT) aerogels were synthesized via an ice-templating (IT) and emulsion-templating (ET) approach, respectively. The resulting two aerogels (rIT-CNT aerogel and rET-CNT aerogel) are similar in their chemical composition but fundamentally different in internal microstructure, crosslinking density and porosity. These fundamental structural differences give rise to substantial efficiency differences in electrical aerogel heating (46 ºC/W for rET-CNT aerogel, 75 ºC/W for rIT-CNT aerogel). Additionally, systematic variation of nanocarbon aerogel microstructure in terms of nanocarbon type (CNT vs reduced-graphene-oxide), envelope density, and nanocarbon graphiticity shows that the Joule-heating efficiency is highly correlated with their thermal conductivities, with aerogels of low thermal conductivities exhibiting the highest Joule-heating efficiencies. A similar relationship and heating behavior are also observed for solar-thermal aerogel heating, an important alternative heating mode, with the aerogels of lowest thermal conductivity (rIT-CNT aerogel) exhibiting a 30% higher efficiency in solar water evaporation, compared to rET-CNT

aerogels. These results demonstrate nanocarbon aerogels' heating properties can be readily tuned and enhanced through structural control alone. The findings therefore provide a new perspective for the design of nanocarbon aerogel for applications where electrical or solar-thermal aerogel heating is important, such as temperature-dependent separation, sorption, sensing, and catalysis applications.

Nanocarbon aerogels have been widely explored as high-performance functional materials in sorption,[1] catalysis,[2] fuel purification,[3, 4] energy storage[5] and sensing.[6] Recently, nanocarbon-based aerogels have also shown great promise for desalination and solar steam evaporation applications, [7, 8] important for the development of new clean water technologies. A highly interesting feature of nanocarbon aerogels, in context of many of these applications, is their potential to be directly heated through the application of an electrical current (Joule-heating)[9, 10] or through solar irradiation (solar thermal energy conversion),[11, 12] e.g. in order to activate desired chemical processes at elevated temperatures, to thermally regenerate materials after use, or to accelerate physical processes such as water evaporation. The 3D interconnected graphitic microstructure of the electrically-conducting aerogel framework enables uniform local electrical heating across the entire porous material, resulting in faster, more efficient and more homogeneous heating, compared to conventional external heating processes (e.g. in an oven or furnace).[9] For instance, it has been shown that a typical reduced graphene oxide (rGO) aerogel can be accurately and repeatedly Joule-heated to a desired temperature at relatively low electrical potentials, high heating efficiency (45°C/W), very fast heating speeds (600 K/min), and low energy consumption.[9] The utility of such nanocarbon aerogel Joule-heating has been demonstrated in first applications. For example, direct resistive Joule-heating has been employed to thermally regenerate functional graphene and CNT aerogels at temperatures between 100-400°C, e.g. in context of highly sensitive gas sensing[6] and adsorptive fuel desulfurization.[4,5] In context of catalysis, Joule-heating was successfully

employed for precise temperature control of Ag/Co_3O_4/Carbon hybrid aerogel catalysts, used for efficient catalytic formaldehyde oxidation at 90 ºC.[13] Direct electro-thermal heating of interconnected 3D nanocarbon networks has also been exploited for polymer curing[14-16] and for the detection of structural damage in polymer nanocomposites through thermal IR imaging.[17] Joule-heating has also proven an energy efficient approach to induce heating in graphene-wrapped polymeric sponges in order to thermally enhance their performance as crude-oil clean-up agents.[18]

Nanocarbon aerogels have also been repeatedly studied as solar thermal conversion materials for solar water evaporation, an emerging technology important in context of water desalination, liquid-phase separation and sterilization applications.[19-21] In this context, heat generation is through absorption of solar light.[22] The heat generated upon light absorption can be utilized to promote water evaporation (solar steam generation).[23] Most solar steam generation methodologies employ porous solar thermal conversion materials that are placed on top of the water surface, so that heat generated from solar irradiation can contribute to water evaporation, overall reducing process duration and lowering energy costs. Nanocarbon aerogels have been investigated in solar water evaporation due to their efficient light absorption (leading to excellent heat conversion efficiencies), ultra-low density (allowing them to be floated on top of the water reservoir), high porosity (enabling water vapor to escape through solar thermal conversion materials) and excellent physico-chemical stability (enabling repeated use).[24] For example, highly porous GO aerogel membranes have shown good solar thermal heating performance under 3 sun artificial solar irradiation, heating up to about 41 °C surface temperature, and exhibiting good thermal conversion efficiencies (~65 %).[20] Further improvements were demonstrated for hybrid GO/CNT/alginate hybrid aerogels that have shown even better thermal conversion efficiencies, reaching local temperatures of around 42 °C under only one sun irradiation (1 $kW \cdot m^{-2}$). The resulting aerogel-based solar thermal conversion materials showed solar water evaporation rates of up to 1.62 $kg \cdot m^{-2} \cdot h^{-1}$ under 1 sun irradiation

- triple that of pure water under the same irradiation conditions.[19] Similar improvements can be achieved, when using nitrogen doped graphene aerogels which have shown solar thermal conversion efficiencies of up to 90 % and evaporation rates of 1.56 $kg \cdot m^{-2} \cdot h^{-1}$ at 1 $kW \cdot m^{-2}$ solar irradiation.[22]

While the Joule-heating and solar-thermal-heating has been studied and optimized for individual nanocarbon aerogel systems, little is known about the more general inter-relationship between nanocarbon aerogel structure and their electrical or solar-thermal heating properties. In this work, Joule-heating based measurements will be explored as straightforward and reliable methodology to measure heating properties of a broad range of 3D nanocarbon networks. The initial focus in this work will lie on CNT aerogels, produced by polymer-assisted ice-templating (IT)[25] and emulsion-templating (ET),[26] to produce two nanocarbon aerogels with similar chemistry but fundamentally different microstructure and porosity. The correlation of nanocarbon aerogel structure and heating behavior will then be further explored through the investigation of nanocarbon aerogels that differ in nanocarbon building block, density and nanocarbon graphiticity. It is then investigated how the structurally-induced differences impact on the aerogels' thermal conductivity and how this is in turn is correlated to the aerogels' functional performance in electrical Joule-heating and solar steam generation.

In order to study the impact of microstructure on aerogel thermal conductivity, two contrasting CNT aerogels were synthesized via an ice-templating (IT) and emulsion-templating (ET) fabrication approach, respectively (rIT-CNT aerogel and rET-CNT aerogel, as depicted in **Figure 1a**). SEM imaging confirms that the two CNT aerogels exhibit very different internal microstructures (Figure 1b, Figure 1c). While the rIT-CNT aerogel presents some larger, micron-sized pockets, likely caused by formation of ice-crystals during aerogel synthesis, its primary structural feature is a comparatively dense, continuous 3D network of highly entangled nanotubes (Figure 1c).

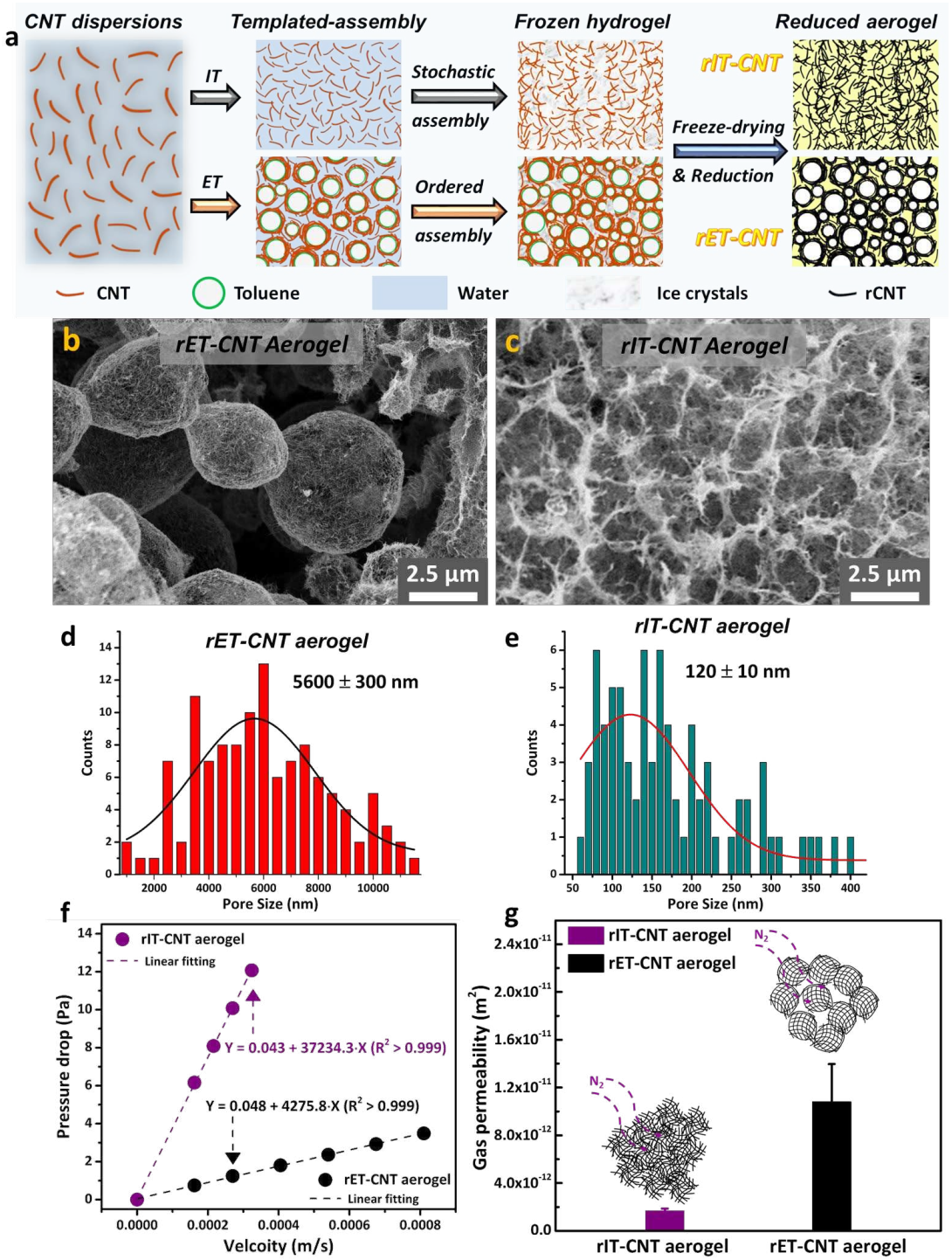

Figure 1. (a) Schematic illustration of the synthesis of nanocarbon aerogels via polymer-assisted ice-templating (rIT-CNT aerogel) and polymer-assisted emulsion-templating (rET-CNT aerogel). (b, c) Microstructure of rET-CNT aerogel and rIT-CNT aerogel as imaged by SEM (sampled from the core region of the monolithic aerogel samples). (d, e) Size distribution of predominant pore type in rET-CNT aerogels and rIT-CNT aerogels, as determined by SEM imaging. (f) Nitrogen gas pressure-drop across the aerogels as function gas velocity for the two aerogels, used to extract through-plane gas permeability values. (g) Through-plane gas permeabilities (in N_2 atmosphere) of the rIT-CNT aerogel and rET-CNT aerogel.

In contrast, the internal microstructure of the rET-CNT aerogels consists of emulsion-templated,

hollow CNT microspheres, that are relatively loosely packed with large open gaps and channels

between them and with a smaller degree of 3D interconnectivity (Figure 1b). SEM indicates that the average size of the gaps and pores in the rET-CNT aerogels is about 5.6 μm (Figure 1d). In contrast, the predominant pore type in the rIT-CNT aerogels stems from the interstitial spaces in the entangled CNT network, with an average pore size substantially smaller (around 0.1 μm) compared to the rET-CNT aerogel (see also pore size distributions, as measured by image analysis in Figure 1d-1e). The denser, more entangled network microstructure of the rIT-CNT aerogels is further indicated by a high, through-volume electrical conductivity of the aerogel (8.0 S/m, **Table 1**), indicating the presence of a highly interconnected 3D network of high crosslinking density. In contrast, the rET-CNT aerogel exhibits an order-of-magnitude lower through-volume electrical conductivity (0.7 S/m, Table 1), suggesting a lower degree of 3D interconnectivity and crosslinking density, in line with the more open microstructure observed by SEM. The pronounced difference in microstructure is also reflected in other bulk aerogel properties, such as gas permeability (Figure 1g). Through-plane nitrogen flow measurements show highly linear gas velocity-pressure drop correlations (both $R^2 > 0.999$, Figure 1f) that enable to extract the steady-state gas permeability values for both aerogel types (Figure 1g). A distinct difference in gas permeability between the two samples is observed, with the rET-CNT aerogel showing an order-of-magnitude larger nitrogen gas permeability (Figure 1g and Table 1), again consistent with the looser, more open microstructure of the rET-CNT aerogel.

Table 1. Selection of aerogel materials characteristics, that confirm pronounced differences in aerogel microstructure of rET-CNT and rIT-CNT aerogels.

Aerogel	Pore size [a] [μm]	Gas permeability [b] [10^{-11} m^2]	Electrical conductivity, σ [c] [S/m]	Thermal conductivity, κ [d] [$W \cdot m^{-1} \cdot k^{-1}$]
rET-CNT aerogel	5.6	1.08	0.7	0.174
rIT-CNT aerogel	0.1	0.11	8.0	0.104

[a]as obtained from SEM images analysis via Image J; [b]as determined by N_2 gas pressure drop measurements at different gas velocities (see also Figures 1f and 1g); [c]through-volume aerogel electrical conductivity; [d] as determined from radial temperature gradients, measured via aerogel Joule heating at 2W power input (see also Experimental).

In terms of other materials characteristics, the two aerogel samples are however very similar (**Table 2**). Both aerogels are formed from the same MWCNT raw material using the same polymer-assisted approach, with the only modification occurring in the templating agent which is completely removed in both cases during the final high-temperature annealing step (see Experimental). The two aerogels are therefore very similar in their basic crosslinking chemistry (for both aerogels based on covalent crosslinking through graphitized polymer residues formed during the annealing step).[29] Both aerogels show very similar, high thermal stability to temperatures up to 555 °C,[27] even in oxidative air atmosphere (an important requisite for many practical thermal applications of nanocarbon aerogels and for the heating experiments conducted in this work, see ESI Figure S1, Table 2). Raman spectra and XRD patterns of the aerogels confirm also very similar graphitic crystallinity and defect concentrations of the CNTs in the aerogels (see ESI Figure S2-S3, Table 2).[28, 29] Nitrogen absorption measurements show that the specific surface areas are also relatively similar, with the surface area of the rET-CNT aerogel only around 20 % different from the rIT-CNT aerogels (see ESI Figure S4, Table 2). The main distinguishing feature between the rIT-CNT and rET-CNT aerogels is therefore their highly contrasting internal structure, making the samples an interesting first model system to investigate Joule-heating characteristics as function of nanocarbon aerogel microstructure.

Table 2. Physico-chemical materials characteristics of rET-CNT aerogel and rIT-CNT aerogel.

Aerogel	Nano-carbon type	Envelope Density [a] [g/cm^3]	Combustion Temperature [b] [°C]	Specific Surface Area [c] [m^2/g]	graphitic crystal domain size [d] [nm]	Raman I_D/I_G ratio [e]
rET-CNT aerogel	rCNT	0.006	555 °C	358	2.23	0.75
rIT-CNT aerogel	rCNT	0.009	555 °C	290	2.44	0.82

[a] ρ represents aerogel envelope density; [b] Nanocarbon combustion temperature, as obtained by TGA in air (see also ESI, Figure S1); [c] specific surface area as obtained by BET analysis (see also ESI, Figure S4); [d] crystal domain size along the stacking direction of the graphitic layers, as estimated from the graphitic (002) XRD peak (see also ESI, Figure S3); [e] Raman I_D/I_G ratio (see also ESI, Figure S2).

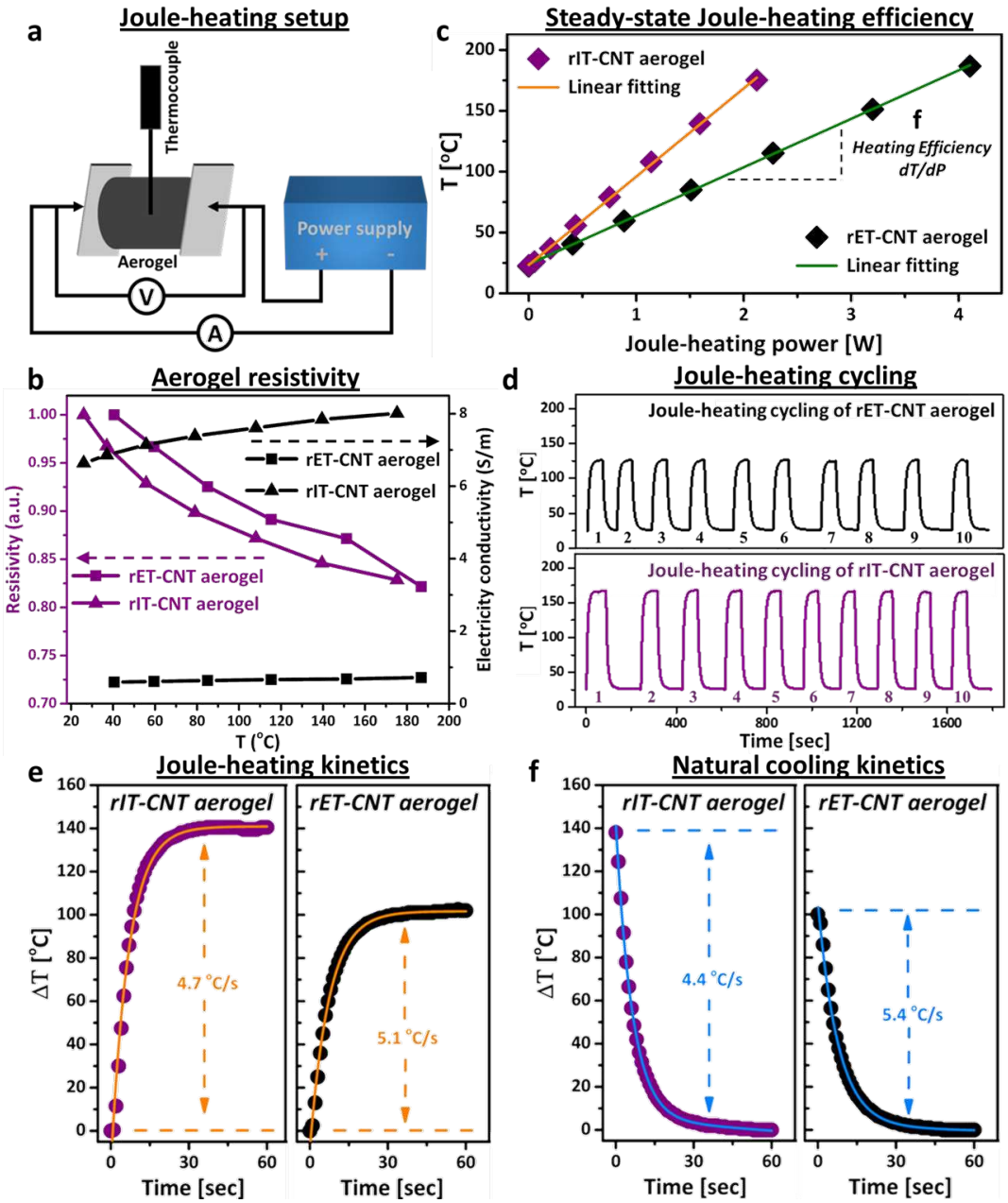

Figure 2. (a) Schematic of a nanocarbon aerogel Joule-heating setup. (b) Electrical properties of rET-CNT and rIT-CNT aerogels: electrical conductivity and relative resistivity as function of Joule-heating temperature. (c) Joule-heating characterization of rET-CNT and rIT-CNT aerogels via current-step experiments: steady-state Joule-heating core temperature as function of electrical power input. (d) Joule-heating cycling of rET-CNT and rIT-CNT aerogels at 2W. (e) Joule-heating kinetics: increase in aerogel core temperature with time (2W electrical power input switched on at t = 0 sec); (f) Natural cooling kinetics: decrease of aerogel core temperature with time (2 W electrical power input switched off at t = 0 sec).

In order to quantitatively measure Joule-heating characteristics, electrical measurements of the aerogels were carried out using a custom-made Joule-heating set-up (**Figure 2a** and ESI Figure S5). All samples were investigated after careful preconditioning at 200 °C (see Experimental) to remove adsorbents (water, ambient volatile impurities) from the nanocarbon surfaces, an

important requisite to ensure repeatability of the Joule-heating measurements (see ESI Figure S6-S7). After preconditioning, both aerogels show highly linear I-V characteristics up to currents of 0.5 A and voltages of 20 V, confirming that the aerogels behave as Ohmic resistors over the current-voltage range investigated (see ESI Figure S8). In the current-voltage range studied here, resistive aerogel Joule-heating to temperature up to 185 °C is observed. Over this temperature range, the aerogels show only relatively minor changes in electrical resistivity (less than 20 % change between room temperature and 185 °C, Figure 2b). Interestingly, aerogel resistivity decreases with increasing temperature, indicating a semiconductor-type behavior (in contrast to the metallic nature of individual MWCNTs),[30] potentially originating from junction resistance effects in the 3D networks and/or incomplete graphitization of polymer residues during the thermal treatment step.

Table 3. Joule-heating characteristics of rET-CNT aerogel and rIT-CNT aerogel collected at a heating power 2W.

Aerogel	Core Temperature T [°C]	Heating Efficiency dT/dP [°C/W]	Heating Rate dT/dt [°C/min]	Cooling Rate -dT/dt [°C/min]
rET-CNT aerogel	114	46	306	324
rIT-CNT aerogel	168	75	282	264

To assess heating efficiency, the aerogels' steady state Joule-heating temperature was measured at different electrical power inputs ($P = I \times V$, Figure 2c and **Table 3**). The resulting Joule-heating plots indicate substantial differences in Joule-heating efficiency (here defined as temperature increase per electrical power input, dT/dP). Specifically, the rIT-CNT aerogel exhibits a more than 60 % larger Joule-heating efficiency (74 °C/W) compared to the rET-CNT aerogel (46 °C/W). This efficiency difference is confirmed by Joule-heating experiments carried out at constant electrical power input. For example, at the same electrical power input of 2W, the rIT-CNT aerogel reaches a significantly higher Joule-heating core temperature (168 ± 8°C, Table 3) compared to the rET-CNT aerogels (114 ± 4°C, Table 3). The stability and

repeatability of the aerogels' Joule-heating characteristics under these temperature conditions is evidenced by highly repeatable Joule-heating cycling (Figure 2d). Differences are also observed for the rate of Joule-heating of the two aerogel samples. When monitoring Joule-heating temperature over time after 'switching-on' an electrical heating current (set to a consistent power input of 2W), both aerogels show extremely fast heating kinetics (up to 300 °C/min), with the rET-CNT aerogels showing slightly faster Joule-heating compared to the rIT-CNT aerogels (Figure 2e, Table 3, ESI Figure S9). Due to the excellent thermal conductivity of the nanocarbon framework, both aerogels also cool down to room temperature extremely fast once the electrical heating current has been 'switched-off' (cooling rates of up to 320 °C/min, Figure 2f, ESI Figure S9). Cooling kinetics for the rET-CNT aerogel are about 20 % faster compared to the rIT-CNT aerogel (Table 3), potentially caused by the more open internal microstructure, promoting heat loss during cooling.[9] The significant differences in efficiency and kinetics clearly demonstrate that aerogel microstructure is a key factor impacting resistive heating behavior.

A likely, important influencing factor in this context is the thermal conductivity of the aerogels. Thermal conductivity will control heat transfer and therefore heat losses to the environment and thereby impact on steady-state Joule-heating temperature.[9, 31, 32] To measure the aerogels' thermal conductivity, the radial temperature gradient of Joule-heated aerogels was analyzed. Specifically, the temperature decline of a Joule-heated aerogel from the aerogel core to the outer surface is measured and the resulting radial gradient used to estimate the aerogel's thermal conductivity (see also Experimental and ESI Figure S10; it has been shown that this approach provides values in good agreement with thermal conductivity values, determined by other methods, such as thermal diffusivity-based approaches[9]). For the two CNT aerogels studied here, the thermal conductivity of the rIT-CNT aerogel is found to be about 70 % smaller than that of the rET-CNT aerogel, likely resulting in reduced heat losses to the environment and

therefore overall higher Joule-heating efficiency for the rIT-CNT aerogel. To further confirm this controlling effect of thermal conductivity, a series of four additional ice-templated aerogels were synthesized. The ice-templating synthesis was modified by changing nanocarbon building block (CNT replaced by GO, sample labelled as rIT-GO aerogel) and thermal reduction treatment (change of reduction atmosphere to N_2 and reduction temperature to 800 °C; samples labelled as rIT-CNT_{N2}, rIT-GO_{N2} and rIT-GO_{800} aerogel respectively). All samples were then characterized in terms of envelope density, electrical conductivity, and thermal conductivity (**Table 4**).

Table 4. Conductivity and Joule-heating characteristics of other ice-templated nanocarbon aerogels.

Aerogel	$\rho^{a)}$ [mg/cm^3]	$\sigma^{b)}$ [S/m]	$\kappa^{c)}$ [W·m^{-1}·k^{-1}]	T $^{d)}$ [°C]	dT/dP $^{e)}$ [°C/W]
rIT-GO aerogel	4.9	8.9	0.152	116	48
rIT-CNT_{N2} aerogel	9.8	7.3	0.135	136	57
rIT-GO_{N2} aerogel	6.4	5.7	0.156	113	46
rIT-GO_{800} aerogel	6.3	9.6	0.125	143	61

[a)]aerogel envelope density; [b)]through-volume aerogel electrical conductivity; [c)]thermal conductivity, as determined from radial temperature gradients, measured via aerogel Joule heating at 2W power input; [d)]Joule-heating temperature at aerogel core, obtained at a heating power of 2W; [e)]Joule-heating efficiency, as determined from current step experiments.

Joule-heating experiments of these additional aerogel samples at an electrical power input of 2W were used to measure steady-state Joule-heating characteristics. As expected, the four additional aerogels show clear differences in Joule-heating efficiency. However, their Joule-heating efficiencies do not correlate with key aerogel characteristics, such as electrical conductivity or envelope density (**Figure 3a** and Figure 3b). However, a very clear correlation emerges when Joule-heating efficiency is plotted as function of thermal conductivity (Figure 3c). The inversely proportional relationship between thermal conductivity and Joule-heating efficiency described above is confirmed and can be qualitatively explained by reduced heat transfer into the environment in aerogels with lower thermal conductivity.[33] The origin for the linear nature of this relationship is not fully clear and requires future investigations. These findings very clearly demonstrate that thermal conductivity is a key factor in determining Joule-

heating characteristics of nanocarbon aerogels. In order to increase Joule-heating efficiency for heating applications (local gas heaters, thermal sorbent regeneration, thermal de-freezing materials),[4, 33, 34] nanocarbon aerogels with relatively low thermal conductivities (here observed for aerogels with denser network structure and high crosslinking density) are likely beneficial. In contrast, for applications where Joule-heating effects need to be minimized (e.g. catalytic supports in fuels cells, battery materials etc.),[5, 35] nanocarbon materials with relatively high thermal conductivity (here observed for aerogels with open microstructure and large pore sizes) are likely a better choice.

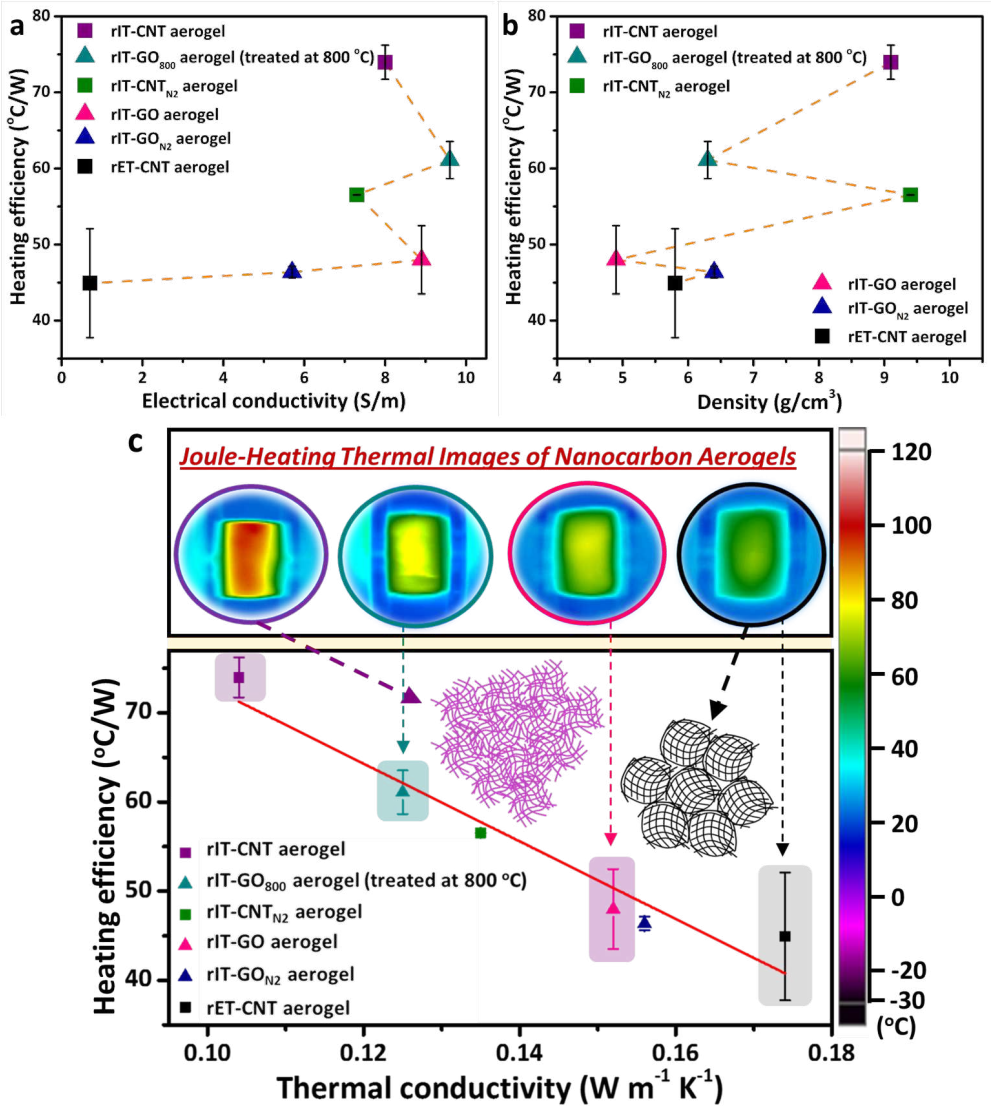

Figure 3. Correlation of aerogel Joule-heating efficiency with different physico-chemical aerogel characteristics. (a) Plot of Joule-heating efficiency vs. aerogel electrical conductivity, (b) Plot of Joule-heating efficiency vs. aerogel envelope density. (c) Linear correlation between Joule-heating efficiency and aerogel thermal conductivity (Inserted thermal images show aerogel surface temperatures at 2W electrical power input).

Differences in thermal aerogel conductivity are also important to tailor functional performance of nanocarbon aerogels in other heating-related applications. As an example, the rET-CNT aerogel and rIT-CNT aerogel were investigated as solar thermal conversion materials (STCM) for solar steam generation applications. Like other nanocarbon aerogels reported in the literature, our rET-CNT and rIT-CNT aerogels exhibit excellent STCM characteristics. Both aerogels show highly efficient light absorption across the whole solar spectrum (more than that 94 % absorbance between 200 nm to 2000 nm), ensuring high solar thermal conversion efficiencies (**Figure 4a**).[19] Contact angle measurements indicate an overall similar, hydrophobic surface character (see ESI Figure 11). While light absorption and surface character are very similar in both aerogels, they exhibit significantly different thermal conductivities (60 % higher thermal conductivity for the rET-CNT aerogel), as discussed above. To assess the impact of this difference on solar heating, cylindrical rET-CNT and rIT-CNT aerogels were placed on a glass surface and heated through light irradiation from the top (one sun solar simulator, see Figure 4b). Upon reaching steady state, the temperature of the aerogels was then thermally imaged perpendicular to the irradiation direction (Figure 4b inset). The resulting thermal images were analyzed via line scans to plot the temperature gradient from the irradiated aerogel top towards the non-irradiated aerogel bottom (Figure 4b). The temperature of the irradiated aerogel top reaches up to 46 °C, comparable to other nanocarbon based aerogels reported in the literature.[19] The 'vertical' temperature gradient between aerogel top and bottom is shallower and plateaus at a higher temperature for the rIT-CNT aerogel. This effect is a direct consequence of the lower thermal conductivity of the rIT-CNT aerogel, resulting in reduced heat dissipation, and hence more effective trapping of solar heat.

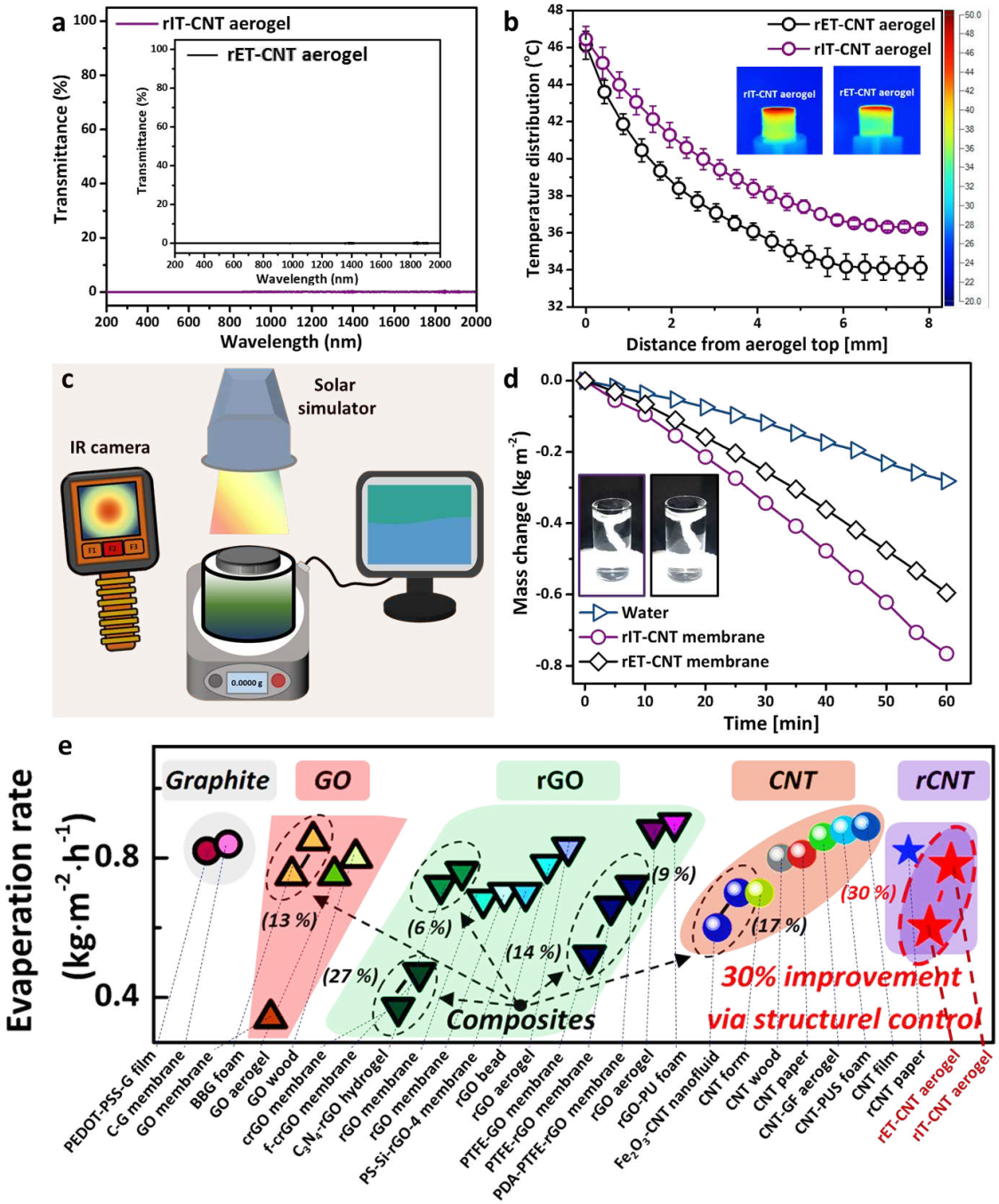

Figure 4. (a) Solar absorption of rIT-CNT aerogel and rET-CNT aerogel. (b) Decline of solar-thermal heating temperature from the aerogels' top surface towards aerogels' bottom surface at 1 sun solar irradiation (aerogels illuminated from the top). (c) Setup for solar steam generation experiments, using rCNT aerogel membranes over a water reservoir. (d) Solar steam generation performance of rET-CNT and rIT-CNT aerogels under one sun irradiation: Water mass change (normalized to surface area of water reservoir) over time for pure water, water with rIT-CNT aerogel, and water with rET-CNT aerogel (Insert shows digital photos of aerogel membranes on top of water reservoir). (e) Solar steam water evaporation rates of different nanocarbon-based solar evaporators under one sun illumination, reported in the literature.

To further investigate this effect, the membrane-shaped aerogels were tested for solar steam generation. (Membrane-shaped rET-CNT and rIT-CNT aerogels were fabricated using the

exact same synthetic parameters as used before, but using smaller volumes of nanocarbon dispersions).[36] For the solar steam evaporation experiment, the aerogel membranes were floated on a water reservoir, irradiated from the top, and the resulting weight loss due to water evaporation monitored through a computer-controlled balance (Figure 4c). Monitoring water evaporation under one sun irradiation shows that the rIT-CNT aerogel exhibits indeed the best solar steam generation performance at a water evaporation rate of 0.78 $kg \cdot m^{-2} \cdot h^{-1}$, i.e. 30 % higher water evaporation efficiency than that of the rET-CNT aerogel and three times higher than that of pure water (Figure 4d).

In terms of absolute values, these evaporation rates are comparable to many carbon-based solar thermal conversion materials reported in the literature (Figure 4e, ESI Table S1).[20, 37-57] Higher water evaporation rates of more than 1 $kg \cdot m^{-2} \cdot h^{-1}$ (like those mentioned in the introduction) are typically achieved through further chemical functionalization of the aerogels (e.g. functionalization with alginate or nitrogen doping)[19, 22] which facilitates the transport of water vapor through the aerogel material. However, our findings clearly show that tailoring the physical microstructure of the aerogel material is an important additional tool to increase solar evaporation efficiencies by at least 30 % as demonstrated here. As observed in the solar steam experiments, the best solar thermal heating efficiencies are observed for the rIT-CNT, i.e. the aerogel with the lower thermal conductivity.

In this work, ice-templating and emulsion-templating approaches were used to form two types of aerogels consisting of CNT 3D networks (rIT-CNT aerogel and rET-CNT aerogel), which have contrasting internal structures and display very different Joule-heating performance. By tuning aerogel microstructure, porosity, and graphiticity and systematically measuring their Joule-heating characteristics (steady-state core temperatures, Joule-heating kinetics), we show that the Joule-heating efficiencies of the materials are highly correlated with their thermal conductivities. In our systematic set of samples, the lowest thermal conductivity and therefore

highest Joule-heating efficiency was displayed by the rIT-CNT aerogel, structurally based on a combination of a more dense, interconnected microstructure and relatively small pore size. Importantly, the principles we discovered are transferable to solar steam generation, where the rIT-CNT aerogel displays a 30% higher water evaporation efficiency than the rET-CNT aerogel under one sun light exposure. The principles we discovered can guide the design of 3D nanocarbon aerogel networks for a wide range of applications, including gas heater, clean water generation or Joule-heating-assisted nanoparticle absorption/desorption.

Experimental Section

Materials: Carboxylic acid functionalized multi-wall carbon nanotubes (CNT, avg. diam. × L, 9.5 nm ×1.5 μm) and polyvinyl alcohol (PVA, Mw: 85000-124000) were purchased from Sigma-Aldrich. Graphene oxide (GO, 0.3 - 0.7 cm diam., carbon: 65-75%, oxygen > 18%, nitrogen < 1%, sulfur < 2%) flakes were purchased from William Blythe Limited. Sucrose, toluene, hydrochloride acid and HPLC were purchased from Scientific UK. All chemicals were used without further purification.

Templated syntheses of nanocarbon aerogels (rIT-CNT, rIT-GO and rET-CNT): Ice-templated nanocarbon aerogels were synthesized via a polymer-assisted procedure as shown in Figure 1a (top row of schematics). Specifically, 0.0375 g PVA and 0.0375 g sucrose were dissolved in 10 mL HPLC water via tip-probe sonication 10 minutes (30% of ultrasound power, model HD2200, Bandelin sonopuls). Then, 0.075 g nanocarbons (CNT or GO starting materials) were added into above mixtures and sonicated 4 times to ensure a high degree of nanocarbon exfoliation (each sonication duration 5 minutes). After each sonication, the nanocarbon mixtures were vigorously agitated for at least 3 minutes to uniformly mix the dispersion (3000 rpm/min). After that, 3.5 mL of the mixtures were added into a bespoke PTFE cylindrical module (I.D. 18 mm, O.D. 20 mm, height 20 mm), followed by freezing in liquid nitrogen and freeze-drying for 24 hours (LABCONCO freeze dryer). The obtained non-reduced nanocarbon aerogels were thermally reduced at 1000 ºC for 2 hours in H_2/N_2 (5% H_2) atmosphere with a heating rate of 5

ºC/min (Carbolite Gero Limited). Final thermally reduced samples are referred to as rIT-GO aerogel and rIT-CNT aerogel, respectively.

A polymer-assisted emulsion-templating approach was employed to prepare a second type of nanocarbon aerogel, with fundamentally different porosity (rET-CNT aerogel, Figure 1a lower row of schematics). An initial aqueous CNT/PVA/sucrose dispersion was prepared using the same synthetic parameters employed for the rIT-CNT aerogel. Then, 2.5 mL toluene were added to this initial aqueous CNT dispersion, followed by the addition of 1 mL 0.1M HCl under agitation to induce the formation of CNT-stabilized water/toluene emulsion. The resulting emulsion was then frozen, freeze-dried and thermally reduced, using the same parameters used for the rIT-CNT aerogel.

In order to produce aerogels with different degree of chemical reduction, IT-GO aerogels were reduced in H_2/N_2 atmosphere at a temperature of 800 ºC (samples labeled as rIT-GO_{800} aerogels), as well as in pure N_2 atmosphere at 1000 °C (labelled as rIT-CNT_{N2} aerogel and rIT-GO_{N2} aerogel). All the IT and ET aerogels were fabricated into the same cylindrical shape and size (diameter ~1.6 cm, height ~1.3 cm), important to reduce error in Joule-heating based property measurements.

Joule-heating measurements: In order to Joule-heat aerogels in a highly controlled manner, the cylindrical aerogel monoliths were inserted into a custom-made, electrically-contactable sample holder (Figure 2a, ESI Figure S5), consisting two circular, aluminum electrodes, held by two moveable, heat-resistant alumina holding blocks. A DC power supply was then connected to the electrodes and was used to control electrical current through the aerogel sample. The current-induced Joule-heating of the aerogel was measured using a thin (0.25 mm diameter) K-type thermocouple (TJC 120 Series, TJC120-CASS-IM025U-250-HMPW-M, Omega UK), inserted into the aerogel core, using a data logger (EL-USB-TC, Lascar Electronics) for continuous temperature read out. To visualize the aerogels' surface temperature a thermal IR camera (Model: Fluke TiR1) was used. All aerogel samples were preconditioned at a Joule-

heating temperature of 200 ºC for 20 minutes to remove adsorbed water and gases. Then current-step experiments were carried out by stepwise increasing electrical current and, hence, Joule-heating temperature of the aerogel samples. At each step, the current was kept constant for 10 minutes before switching to the next current step (see ESI Figure S6-S7). These current-step experiments were used to measure the aerogels' Joule-heating response at different electrical power inputs.

Measurement of aerogel thermal conductivity through Joule-heating experiments: At constant electrical current input, the Joule-heating temperature of an aerogel at the aerogel core will be considerably higher than at the aerogel surface due to constant heat loss at the aerogel surface. The difference between the monolith core and surface temperature (i.e. the degree of heat loss) is crucially dependent on the thermal conductivity of the aerogel. The radial core-to-surface temperature gradient (Figure S10 for representative data from this work) can be analyzed by a simplified model for one-dimensional heat conduction in cylinders with homogeneous, internal energy generation[9]:

$$T=C_{rad}\cdot r^2+T_{surf} \qquad \text{(Equation 1)}$$

$$\kappa=q/(4\cdot C_{rad}) \qquad \text{(Equation 2)}$$

where r is the distance from the aerogel core (mm); T is the measured temperature at distance r (ºC); q is the Joule-heating energy density (W/m^3); T_{surf} is the surface temperature; C_{rad} is the corresponding quadratic fit parameters (K/m^2); κ is the thermal conductivity of the aerogel (W·m^{-1}·K^{-1}), and q is the Joule-heating energy density (W/m^3, estimated as ratio of electrical power input over aerogel monolith volume).[9] To determine aerogel thermal conductivity, the radial Joule-heating gradients of cylindrical aerogels (diameter ~1.6 cm, height ~1.3 cm) were determined at an electrical power input of 2W, measuring Joule-heating temperatures at different radial distances from the aerogel core via a thermal couple. Thermal conductivity values were extracted from the resulting temperature gradient plots through quadratic fitting

(Equations 1 and 2). All Joule-heating experiments were carried out at least three times and exhibited high reproducibility.

Material characterization: Thermogravimetric analysis (TGA) was measured in air atmosphere to analyze the thermal stability of nanocarbon aerogels, using 10 ºC/min ramping rate from 20 to 850 ºC (TGA Q600 model, USA). Brunauer-Emmett-Teller (BET) surface area measurements were conducted using a Micromeritics TriStar 3000 instrument. All measured samples were degassed under N_2 gas atmosphere at 110 ºC for 3 hours prior to analysis. Scanning electron microscopy (SEM) images were taken using a Nova NanoSEM 450 with an accelerating voltage of 3 kV. Thermal images were taken using Fluke TiR1 thermal camera and were analyzed via Fluke Connect software. Raman spectra were measured using a Renishaw InVia with an excitation laser wavelength of 532 nm between 400 and 4000 cm^{-1}. X-ray diffraction (XRD) was conducted on a Bruker D2 Phaser Diffractometer. The through-plane gas permeability of nanocarbon aerogels was tested using an in-house built setup with a flow controller (HFC-202, Teledyne Hastings, UK) and a differential pressure sensor (PX653, Omega, UK). Aerogel light absorption (wavelength range from 200 nm to 2000 nm) was measured using a UV/VIS/NIR spectrometer (Lambda 950, PerkinElmer). Static water contact angles were tested using a drop-shape analysis device (OCA 25, Dataphysics UK). Solar steam generation was measured using a solar simulator (Newport Co.) under 1 sun solar radiation, using a digital balance (uncertainty of ± 0.001 g, Ohaus, Mettler Toledo) to measure the mass change over time.

Supporting Information

Supporting Information is available from the Wiley Online Library or from the author.

Acknowledgements

The authors would appreciate the China Scholarship Council and University of Leeds for the funding supports.

Received: ((will be filled in by the editorial staff))
Revised: ((will be filled in by the editorial staff))
Published online: ((will be filled in by the editorial staff))

References

[1] W. Wan, R. Zhang, W. Li, H. Liu, Y. Lin, L. Li, Y. Zhou, *Environ. Sci. Nano* **2016,** *3*, 107.
[2] K.Q. Lu, X. Xin, N. Zhang, Z.R. Tang, Y.J. Xu, *J. Mater. Chem. A* **2018,** *6*, 4590.
[3] D. Xia, H. Li, J. Mannering, P. Huang, X. Zheng, A. Kulak, D. Baker, D. Iruretagoyena, R. Menzel, *Adv. Funct. Mater* **2020**, 2002788.
[4] D. Xia, H. Li, P. Huang, J. Mannering, U. Zafar, D. Baker, R. Menzel, *J. Mater. Chem. A* **2019,** *7*, 24027.
[5] J. Mao, J. Iocozzia, J. Huang, K. Meng, Y. Lai, Z. Lin, *Energ. Environ. Sci.* **2018,** *11*, 772.
[6] F. Yavari, Z. Chen, A.V. Thomas, W. Ren, H.M. Cheng, N. Koratkar, *Sci. Rep.* **2011,** *1*, 1.
[7] Y. Yang, R. Zhao, T. Zhang, K. Zhao, P. Xiao, Y. Ma, P.M. Ajayan, G. Shi, Y. Chen, *Acs Nano* **2018,** *12*, 829.
[8] H. Ren, M. Tang, B. Guan, K. Wang, J. Yang, F. Wang, M. Wang, J. Shan, Z. Chen, D. Wei, *Adv. Mater.* **2017,** *29*, 1702590.
[9] R. Menzel, S. Barg, M. Miranda, D.B. Anthony, S.M. Bawaked, M. Mokhtar, S.A. Al-Thabaiti, S.N. Basahel, E. Saiz, M.S.P. Shaffer, *Adv. Funct. Mater.* **2015,** *25* (1), 28.
[10] P. Hu, J. Lyu, C. Fu, W.B. Gong, J. Liao, W. Lu, Y. Chen, X. Zhang, *Acs nano* **2019,** *14*, 688.
[11] D.D. Qin, Y.J. Zhu, F.F. Chen, R.L.Yang, Z.C. Xiong, *Carbon* **2019,** *150*, 233.
[12] P. Mu, Z. Zhang, W. Bai, J. He, H. Sun, Z. Zhu, W. Liang, A. Li, *Adv. Energy Mater.* **2019,** *9*, 1802158.
[13] K. Wang, Y. Zeng, W. Lin, X. Yang, Y. Cao, H. Wang, F. Peng, H. Yu, *Carbon* **2020***, 167, 709*.
[14] B. Mas, J.P. Fernández-Blázquez, J. Duval, H. Bunyan, J.J. Vilatela, *Carbon* **2013,** *63*, 523.
[15] T. Xia, D. Zeng, Z. Li, R.J. Young, C. Vallés, I.A. Kinloch, *Compos. Sci. Technol.* **2018,** *164*, 304.
[16] C. Wang, W. Ping, Q. Bai, H. Cui, R. Hensleigh, R.Wang, A.H. Brozena, Z. Xu, J. Dai, Y. Pei, *Science* **2020,** *368*, 521.
[17] R.G. De Villoria, N. Yamamoto, A. Miravete, B.L. Wardle, *Nanotechnology* **2011,** *22*, 185502.
[18] J. Ge, L.A. Shi, Y.C. Wang, H.Y. Zhao, H.B. Yao, Y.B. Zhu, Y. Zhang, H.W. Zhu, H.A. Wu, S.H. Yu, *Nat. Nanotechnol.* **2017,** *12*, 434.
[19] X. Hu, W. Xu, L. Zhou, Y. Tan, Y. Wang, S. Zhu, J. Zhu, *Adv. Mater.* **2017,** *29*, 1604031.
[20] Y. Fu, G. Wang, T. Mei, J. Li, J. Wang, X. Wang, *Acs Sustain. Chem. Eng.* **2017,** *5*, 4665.
[21] Y. Fu, G. Wang, X. Ming, X. Liu, B. Hou, T. Mei, J. Li, J. Wang, X. Wang, *Carbon* **2018,** *130*, 250.
[22] B. Huo, D. Jiang, X. Cao, H. Liang, Z. Liu, C. Li, J. Liu, *Carbon* **2019,** *142*, 13.
[23] Z. Wang, T. Horseman, A,P. Straub, N.Y. Yip, D. Li, M. Elimelech, S. Lin, *Sci. Adv.* **2019,** *5*, eaax0763.

[24] Z. Deng, J. Zhou, L. Miao, C. Liu, Y. Peng, L. Sun, S. Tanemura, *J. Mater. Chem. A* **2017,** *5*, 7691.
[25] C. Li, Z.Y. Wu, H.W. Liang, J.F. Chen, S.H. Yu, *Small* **2017,** *13*, 1700453.
[26] S. Barg, F.M. Perez, N. Ni, P. do Vale Pereira, R.C. Maher, E. Garcia-Tunon, S. Eslava, S. Agnoli, C. Mattevi, E. Saiz, *Nat. Commun.* **2014,** *5*, 4328.
[27] N. Nguyen, S. Zhang, A. Oluwalowo, J.G. Park, K. Yao, R. Liang, *Acs Appl. Mater. Inter.* **2018,** *10*, 27171.
[28] X. Chen, H. Liu, Y. Zheng, Y. Zhai, X. Liu, C. Liu, L. Mi, Z. Guo, C. Shen, *Acs Appl. Mater. Inter.* **2019,** *11*, 42594.
[29] C. Zhang, B. Ma, Y. Zhou, *ChemCatChem* **2019,** *11*, 5495.
[30] M. Mujahid, R.U. Khan, M. Mumtaz, S.A. Soomro, S. Ullah, *Ceram. Int.* **2019,** *45*, 8486.
[31] Y. Zeng, T. Li, Y. Yao, T. Li, L. Hu, A. Marconnet, *Adv. Funct. Mater.* **2019,** *29*, 1901388.
[32] T. Li, A.D. Pickel, Y. Yao, Y. Chen, Y. Zeng, S.D. Lacey, Y. Li, Y. Wang, J. Dai, Y. Wang, *Nat. Energy* **2018,** *3*, 148.
[33] M. Liu, H. Wang, S. Wu, Y. Wang, S. Qiu, S. Zhang, C. Bao, *Appl. Therm. Eng.* **2020**, 115319.
[34] Q. Zhang, Y. Yu, K. Yang, B. Zhang, K. Zhao, G. Xiong, X. Zhang, *Carbon* **2017,** *124*, 296.
[35] Y. Yang, R. Dong, Y. Zhu, H. Li, H. Zhang, X. Fan, H. Chang, *Chem. Eng. J.* **2020,** *381*, 122749.
[36] T. Gao, Y. Li, C. Chen, Z. Yang, Y. Kuang, C. Jia, J. Song, E.M. Hitz, B. Liu, H. Huang, *Small Methods* **2019,** *3*, 1800176.
[37] V. Kashyap, A. Al-Bayati, S.M. Sajadi, P. Irajizad, S.H. Wang, H. Ghasemi, *J. Mater. Chem. A* **2017,** *5*, 15227.
[38] F. Tao, Y. Zhang, B. Wang, F. Zhang, X. Chang, R. Fan, L. Dong, Y. Yin, *Sol. Energ. Mater. Sol. C.* **2018,** *180*, 34.
[39] J. Yang, Y. Pang, W. Huang, S.K. Shaw, J. Schiffbauer, M.A. Pillers, X. Mu, S. Luo, T. Zhang, Y. Huang, *Acs Nano* **2017,** *11*, 5510.
[40] B. Bai, X. Yang, R. Tian, W. Ren, R. Suo, H. Wang, *Appl. Therm. Eng.* **2019,** *163*, 114379.
[41] X. Luo, C. Huang, S. Liu, J. Zhong, *Int. J. Energ. Res.* **2018,** *42*, 4830.
[42] H. Su, J. Zhou, L. Miao, J. Shi, Y. Gu, P. Wang, Y. Tian, X. Mu, A. Wei, L. Huang, *Sustain. Mater. Technol.* **2019,** *20*, e00095.
[43] G. Cheng, X. Wang, X. Liu, Y. He, B.V. Balakin, *Sol. Energy* **2019,** *194*, 415.
[44] X. Feng, J. Zhao, D. Sun, L. Shanmugam, J.K. Kim, J. Yang, *J. Mater. Chem. A* **2019,** *7*, 4400.
[45] X. Deng, Q. Nie, Y. Wu, H. Fang, P. Zhang, Y. Xie, *Acs Appl. Mater. Inter.* **2020,** *12*, 26200.
[46] L. Huang, J. Pei, H. Jiang, X. Hu, *Desalination* **2018,** *442*, 1.
[47] X. Ming, A. Guo, Q. Zhang, Z. Guo, F. Yu, B. Hou, Y. Wang, K.P. Homewood, X. Wang, *Carbon* **2020,** *167*, 285.
[48] G. Wang, Y. Fu, A. Guo, T. Mei, J. Wang, J. Li, X. Wang, *Chem. Mater.* **2017,** *29*, 5629.
[49] W. Chen, C. Zou, X. Li, H. Liang, *Desalination* **2019,** *451*, 92.
[50] Z.C. Xiong, Y.J. Zhu, D.D. Qin, F.F. Chen, R.L. Yang, *Small* **2018,** *14*, 1803387.
[51] Q. Gan, T. Zhang, R. Chen, X. Wang, M. Ye, *Acs Sustain. Chem. Eng.* **2019,** *7*, 3925.
[52] X. Wang, Y. He, X. Liu, J. Zhu, *Powder Technol.* **2017,** *321*, 276.
[53] L. Shi, Y. Wang, L. Zhang, P. Wang, *J. Mater. Chem. A* **2017,** *5*, 16212.
[54] S. Liu, C. Huang, X. Luo, Z. Rao, *Appl. Therm. Eng.* **2018,** *142*, 566.
[55] Y. Wang, C. Wang, X. Song, S.K. Megarajan, H. Jiang, *J. Mater. Chem. A* **2018,** *6*, 963.

[56] R. Hu, J. Zhang, Y. Kuang, K. Wang, X. Cai, Z. Fang, W. Huang, G. Chen, Z. Wang, *J. Mater. Chem. A* **2019,** *7*, 15333.
[57] Z. Yin, H. Wang, M. Jian, Y. Li, K. Xia, M. Zhang, C. Wang, Q. Wang, M. Ma, Q.S. Zheng, *Acs Appl. Mater Inter.* **2017,** *9*, 28596.

Tuning set of nanocarbon aerogels' heating properties via structural control is specially investigated for revealing their potential structure-property correlation (which is verified by two completely different heating approaches: Joule-heating and solar thermal heating), that the lowest thermal conductivities of nanocarbon aerogels leading to the highest Joule-heating efficiencies. This correlation is also transferrable to water steam generation via solar thermal heating.

Keyword Nanocarbon aerogels, tunable microstructures, thermal properties, Joule-heating, solar steam generation

D. Xia,* Y. Xu, J. Mannering, X. Ma, M. Ismail, D. Borman, D. Baker, M. Pourkashanian and R. Menzel

Tuning the Electrical and Solar-Thermal Heating Efficiencies of Nanocarbon Aerogels

ToC Figure

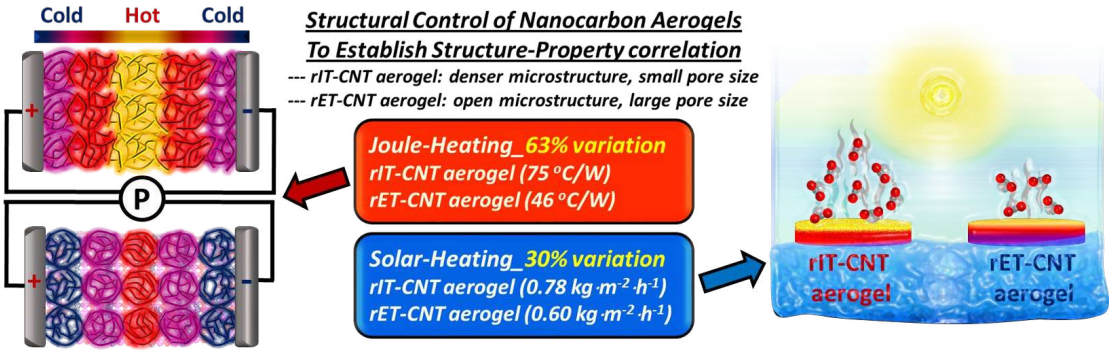

Supporting Information

Tuning the Electrical and Solar-Thermal Heating Efficiencies of Nanocarbon Aerogels

Dong Xia, Yifei Xu, Jamie Mannering, Xiaolong Ma, Mohammed Ismail, Duncan Borman, Daniel Baker, M. Pourkashanian and Robert Menzel*

Materials Characterizations

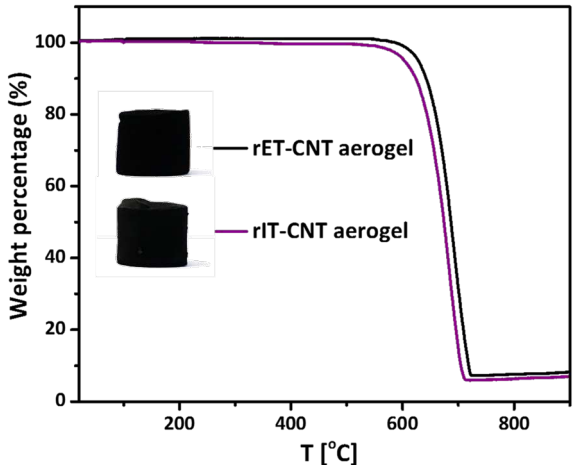

Figure S1. TGA measurements in air atmosphere of rET-CNT and rIT-CNT aerogels. Inserts are digital photos of aerogels.

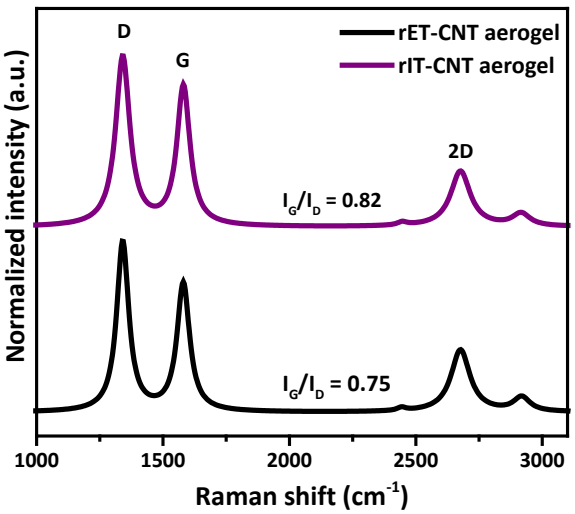

Figure S2. Raman spectra of rET-CNT and rIT-CNT aerogels.

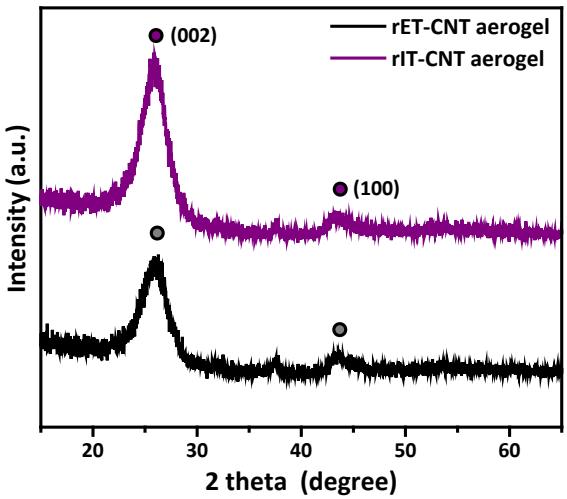

Figure S3. XRD diffraction patterns of rET-CNT and rIT-CNT aerogels

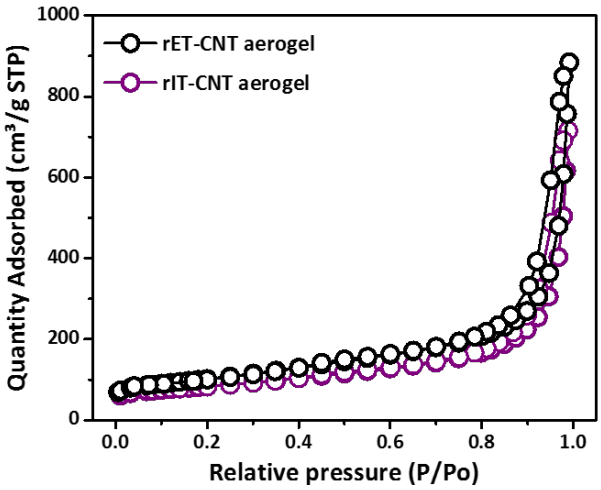

Figure S4. BET adsorption/desorption curves of rET-CNT and rIT-CNT aerogels.

Joule-Heating Experiments

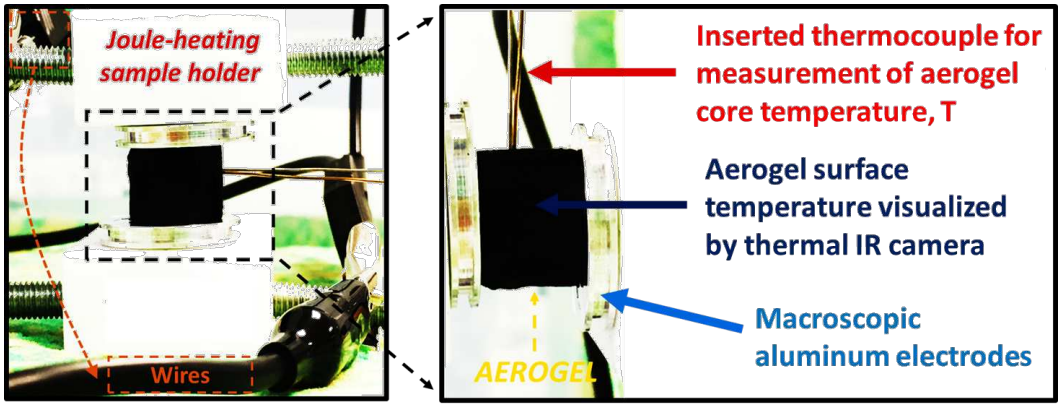

Figure S5. Digital photograph of Joule-heating sample holder.

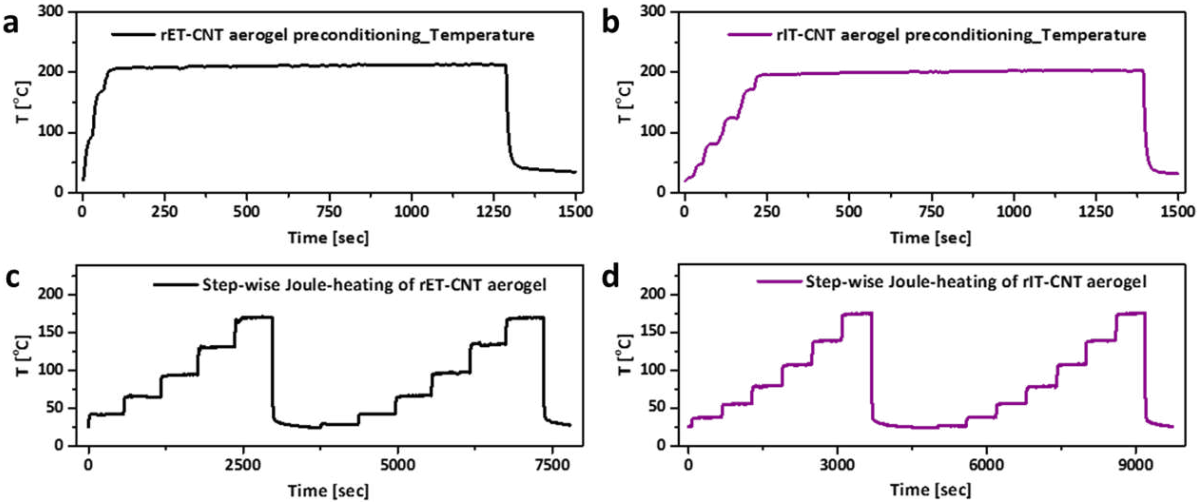

Figure S6. (a-b) Joule-heating preconditioning of rET-CNT aerogel and rIT-CNT aerogel at 200 ºC for 20 minutes. (c-d) Stepwise Joule-heating of rET-CNT aerogel and rIT-CNT aerogel (Each step maintained for 10 minutes).

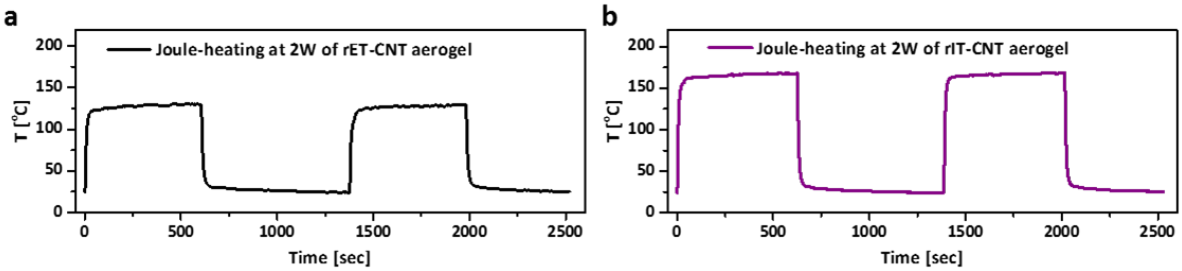

Figure S7. Maintaining for 10 minutes of the rET-CNT aerogel (a) and the rIT-CNT aerogel (b) at 2W Joule-heating.

The detailed Joule-heating procedures of rIT-CNT aerogel and rET-CNT aerogel are presented in Figure S6. Figure S6a and S6b show aerogels' preconditioning to remove impurities (e.g. adsorbed water and gases) for 20 minutes. After preconditioning, both the rCNT aerogels can carry out stable and repeatable Joule-heating measurements (Figure S6c-S6d). Figure S7a and S7b indicate that both the rCNT aerogels exhibit outstanding Joule-heating performance, which can be repeated heating up to high temperature with only 2W power input and kept stable Joule heating temperature over long time.

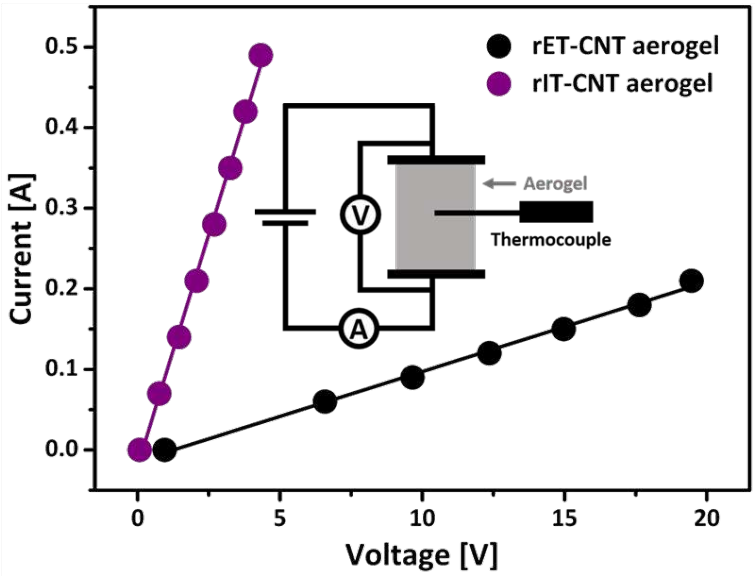

Figure S8. Electrical properties of rET-CNT and rIT-CNT aerogels: (c) I-V curves;

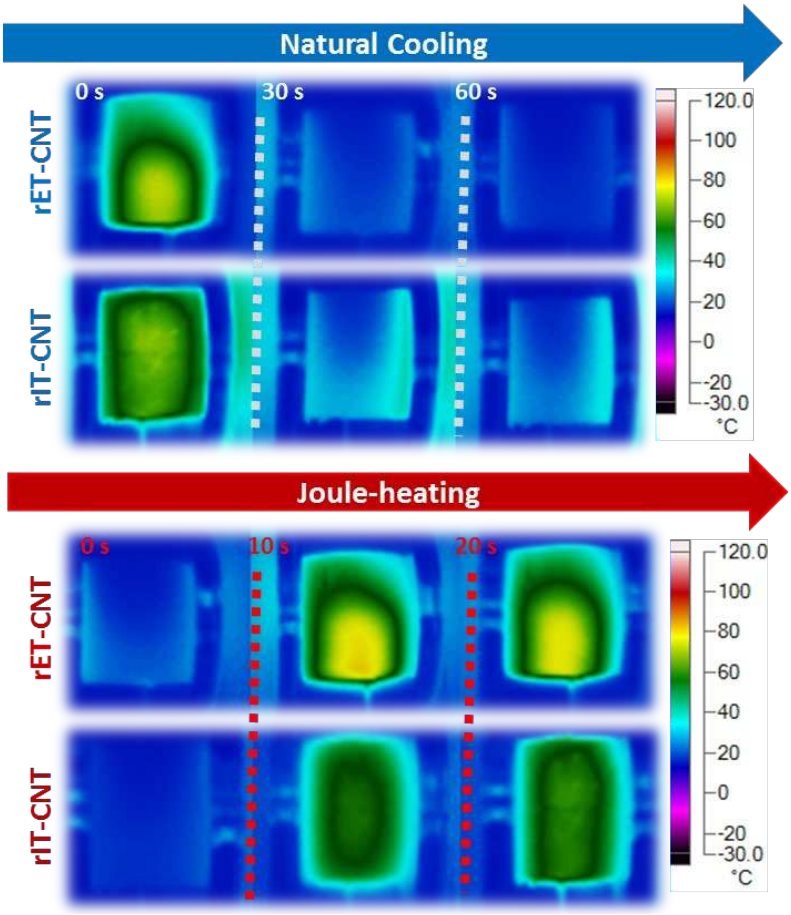

Figure S9. (a) Cooling thermal images of Joule-heating rET-CNT and rIT-CNT aerogels at core temperature 150 ºC, and (b) thermal images of switching on the power to heat up aerogels to core temperature 150 ºC.

In the interest of vision-directly understanding the heating efficiency strictly corresponds with thermal conductivity of nanocarbon aerogels, thermal images were taken for comparison. When the power is off and let the aerogel cool down, counting time internal to take instant cooling pictures from core temperature at 150 ºC (Figure S9a). Judging from the thermal images, rET-CNT aerogel showed the fastest cooling speed due to its high thermal conductivity. On the contrary way, after cooling down to room temperature then switch on the power supply to take instant thermal images again (kept at same power to reach 150 ºC, Figure S9b). Predictably, the rET-CNT aerogel exhibited more quicker thermal transmission effect only took around 10s, this phenomenon explains why the heating efficiency of the rET-CNT aerogel was lower, which directly correlates with its higher thermal conductivity (Figure S9).

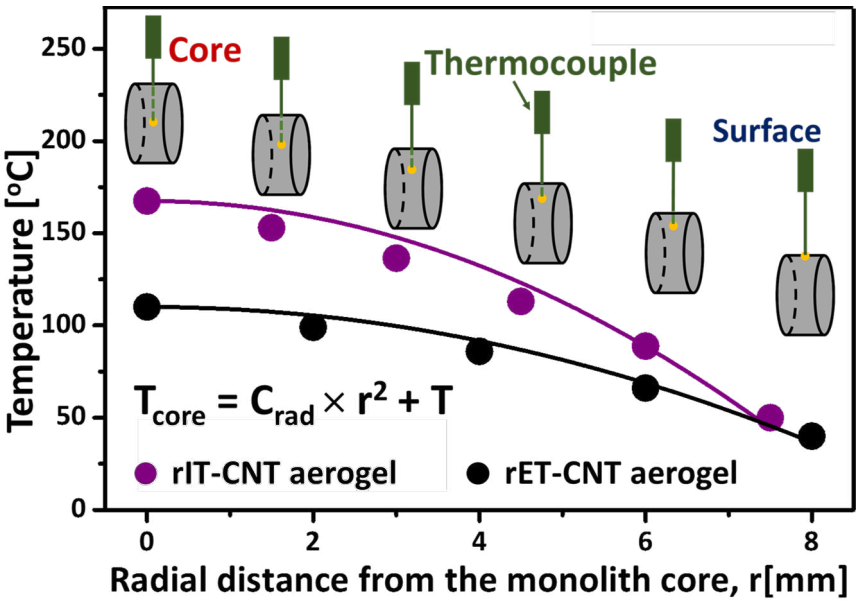

Figure S10. Radial temperature gradient of rET-CNT aerogel and rIT-CNT aerogel, Joule-heated at inputs of electrical power 2W.

Solar Steam Generation

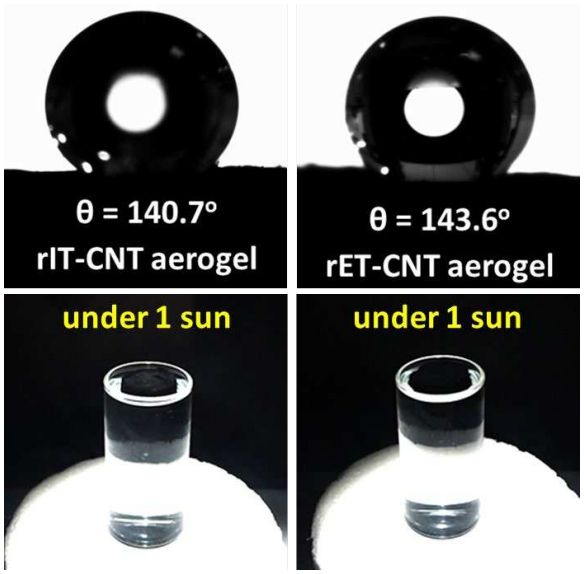

Figure S11. Contact angles and digital images of rIT-CNT aerogel membrane and rET-CNT aerogel membrane under one sun on the top of water.

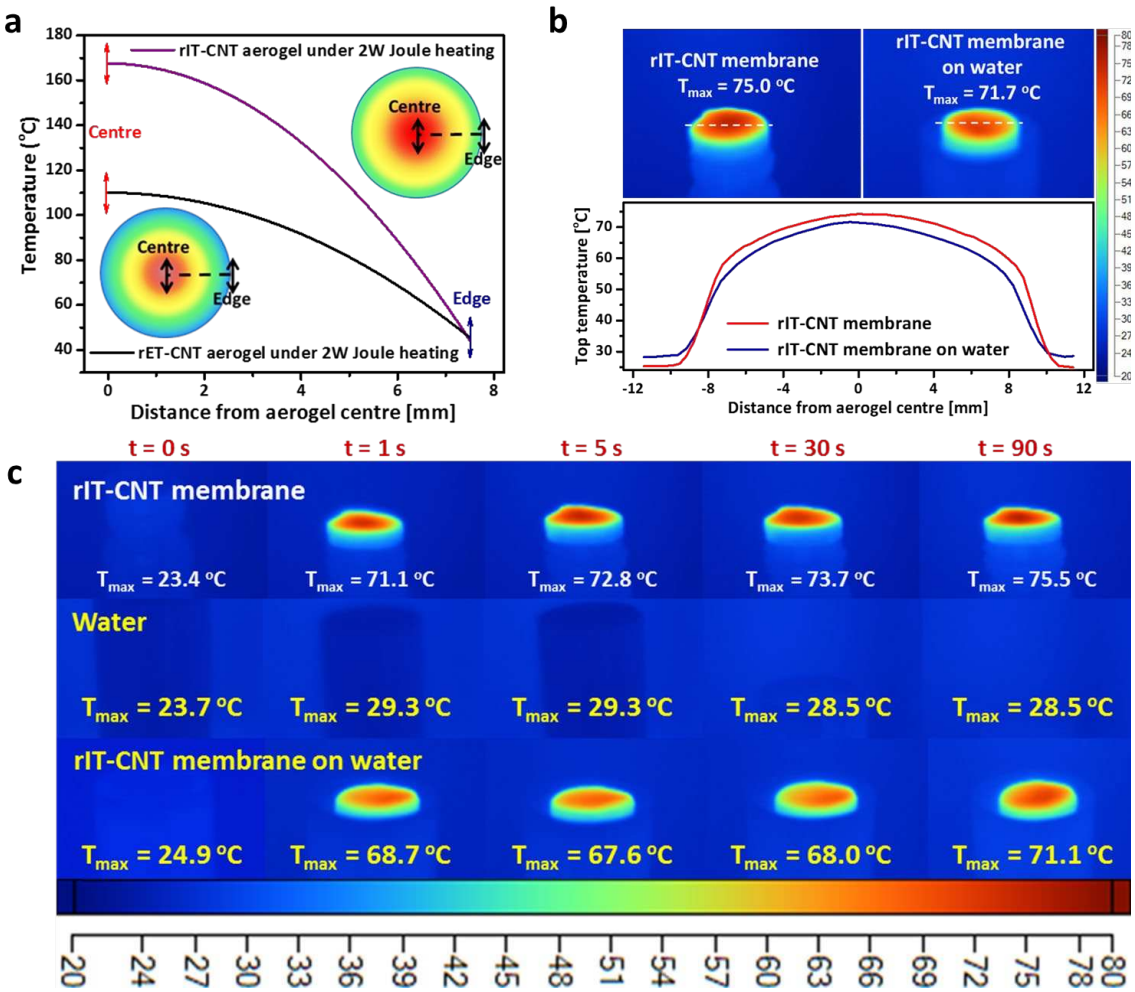

Figure S12. (a) Joule-heating temperature distributions of rIT-CNT aerogel and rET-CNT aerogel from center to edge at power 2W. (b) Thermal images of rIT-CNT membrane on or not on water at lighting time 300s, and the corresponding axis temperature distributions. (c) Thermal images of pure water, rIT-CNT membrane, and rIT-CNT membrane on the top of water at different time interval under one sun illumination.

As shown in Figure S12a, the Joule-heating temperature distributions from the aerogel center to edge is in line with the thermal conductivities, namely the rIT-CNT aerogel will trap more heat under identical conditions, owing to its low thermal conductivity. Time-dependent thermal images of the rIT-CNT aerogel placing on or not on water and the pure water (as blank experiments) indicated that blank water had small temperature variations over the lighting time (Figure S12c), while the surface temperature of aerogel surged up significantly even directly floating on water. For example, the maximum surface temperature of rIT-CNT aerogel on water reached up to 68.7 °C only within 1s solar lighting exposure, verifying that aerogels are fast to generate heat. An important discovery was that the rIT-CNT aerogel experienced 3.3 °C

fluctuation at stable light expose, indicating efficient heat conducting from aerogel to water for executing steam evaporation (Figure S12b).

Table S1. Solar steam generation performance comparison under one sun illumination between nanocarbon-based materials reported from literature and this study.

Solar evaporators	Nanocarbon types	Evaporator Compositions	Water evaporation rate [$kg \cdot m^{-2} \cdot h^{-1}$]	Reference
PEDOT-PSS-G film	Graphite	poly(3,4-ethylenedioxythiophene)–poly(styrenesulfonate)/Graphite	0.82	[37]
C-G membrane	Graphite	Semipermeable collodion/Graphite	0.84	[38]
GO membrane	GO	GO	0.34	[39]
BBG-0.6 foam	GO	Blue brick/GO	0.75	[40]
BBG-1.2 foam	GO	Blue brick/GO	0.85	[40]
GO aerogel	GO	GO	~0.75	[20]
GO-Wood	GO	GO/Wood	~0.80	[41]
crGO membrane	rGO	rGO/Hydrazine	0.37	[39]
f-crGO membrane	rGO	rGO/Hydrazine/Nitric acid	0.47	[39]
C_3N_4-rGO-9 hydrogel	rGO	Graphic C_3N_4/rGO	0.76	[42]
C_3N_4-rGO-1.5 hydrogel	rGO	Graphic C_3N_4/rGO	0.72	[42]
rGO membrane	rGO	rGO	0.68	[55]
rGO membrane	rGO	rGO	~0.70	[43]
PS-Si-rGO-4 membrane	rGO	Polystyrene/rGO	0.7	[53]
rGO bead	rGO	rGO	0.78	[44]
rGO aerogel	rGO	rGO	0.83	[45]
PTFE-GO membrane	GO	Polytetrafluoroethylene/GO	0.52	[46]
PTFE-rGO membrane	rGO	Polytetrafluoroethylene/rGO	0.66	[46]
PDA-PTFE-rGO membrane	rGO	Polydopamine/PTFE/rGO	0.72	[46]
rGO aerogel	rGO	Sodium alginate/rGO	~0.88	[47]
rGO-PU foam	rGO	rGO/Polyurethane	0.90	[48]
Fe_3O_4/CNT-1 nanofluid	CNT	CNT/Fe_3O_4	~0.60	[49]
Fe_3O_4/CNT-10 nanofluid	CNT	CNT/Fe_3O_4	~0.70	[49]
CNT foam	CNT	CNT	~0.70	[57]
CNT-Wood	CNT	CNT/Wood	~0.80	[41]
CNT paper	CNT	Filter paper/CNT	0.81	[50]
CNT-GF aerogel	CNT	Glass fiber/CNT	0.86	[56]

CNT-PUS foam	CNT	CNT/Polyurethane sponge	0.88	[51]
CNT film	CNT	CNT	0.89	[52]
rCNT paper	rCNT	rCNT	0.82	[54]
rET-CNT aerogel	rCNT	rCNT	0.60	Here
rIT-CNT aerogel	rCNT	rCNT	0.78	Here